



Nitrogen-doped porous carbons by conversion of azo dyes especially in the case of tartrazine

Zhong Jie Zhang ^{a,b}, Chong Chen ^b, Peng Cui ^{b,*}, Xiang Ying Chen ^{b,*}

^a College of Chemistry & Chemical Engineering, Anhui Province Key Laboratory of Environment-friendly Polymer Materials, Anhui University, Hefei 230039, Anhui, PR China

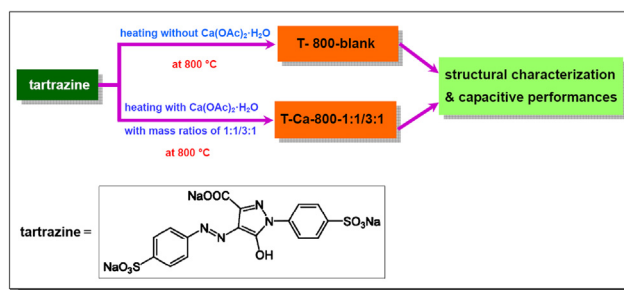
^b School of Chemical Engineering, Anhui Key Laboratory of Controllable Chemistry Reaction & Material Chemical Engineering, Hefei University of Technology, Hefei 230009, Anhui, PR China



HIGHLIGHTS

- A direct carbonization method was developed for nitrogen-doped porous carbon.
- Tartrazine can serve as not only carbon source but also as nitrogen source.
- High surface areas and pore volumes are achieved with $\text{Ca}(\text{OAc})_2 \cdot \text{H}_2\text{O}$.
- The carbon samples exhibit excellent capacitive behaviors.

GRAPHICAL ABSTRACT



ARTICLE INFO

Article history:

Received 15 March 2013

Received in revised form

22 April 2013

Accepted 1 May 2013

Available online 28 May 2013

Keywords:

Tartrazine

Porous carbon

Template

Supercapacitors

ABSTRACT

Nitrogen-doped porous carbons possessing high surface areas and large pore volumes have been prepared by directly heating the mixture of tartrazine and $\text{Ca}(\text{OAc})_2 \cdot \text{H}_2\text{O}$ at 800 °C especially without further physical or chemical activation, where $\text{Ca}(\text{OAc})_2 \cdot \text{H}_2\text{O}$ serves as the hard template to regulate the surface area and pore structures. It reveals that the addition of $\text{Ca}(\text{OAc})_2 \cdot \text{H}_2\text{O}$ can remarkably improve the surface area and total pore volume. The T-Ca-800-3:1 sample displays the highest BET surface area as $1669 \text{ m}^2 \text{ g}^{-1}$ and largest total pore volume $0.85 \text{ cm}^3 \text{ g}^{-1}$, which is much larger than those without adding $\text{Ca}(\text{OAc})_2 \cdot \text{H}_2\text{O}$. Furthermore, it exhibits excellent capacitive performances, including high specific capacitance (ca. 224.3 F g^{-1} at 0.5 A g^{-1}), good rate capability (the retention of 42.6% at 60 A g^{-1}) and good cycling stability (the retention of 92.3% within 5000 cycles).

© 2013 Elsevier B.V. All rights reserved.

1. Introduction

Along with the increasing power demands of energy storage systems in the 21st century, supercapacitors have attracted much attention due to their pulse power supply, long cycle life ($>100,000$ cycles), and high dynamic of charge propagation [1–3]. Among the

reported electrode materials, carbon materials have gained considerable interest because of high electrical conductivity, low cost and multiple forms and allotropes, as well as broad chemical stability in acidic or basic solutions [4,5]. More importantly, Simon et al. found that electrochemical double layer capacitors (EDLCs) are able to operate from -50 – 100 °C on the base of the combination of exohedral nanostructured carbon (nanotubes and onions) electrode and a eutectic mixture of ionic liquids [6]. Consequently, using carbon as the active material, EDLCs represent more than 80% of the commercially manufactured ECs today [7].

* Corresponding authors. Tel./fax: +86 551 2901450.

E-mail addresses: zhangj0603@126.com (Z.J. Zhang), cuipeng@hfut.edu.cn (P. Cui), cxyhfut@gmail.com (X.Y. Chen).

Among the carbon electrodes, porous carbons are of great importance especially due to their high surface area and large pore volume, providing an extensively large electrode/electrolyte interface for charge storage [8]. Xu et al. prepared porous carbons by direct carbonization of poly(vinylidene chloride) (PVDC) without adding any templates, having BET surface area about $1200 \text{ m}^2 \text{ g}^{-1}$ [9]. However, in most cases, hard/soft templates are commonly indispensable for preparing porous carbons. For example, templating with zeolites, silica or silicates can yield micro/meso/macropores with a narrow pore size distribution, but such *ex-situ* template methods are both expensive and inefficient, requiring rigorous etching with HF or KOH to remove the templates [10]. Alternatively, other kinds of hard templates, including MgO [11], $\text{Mg}(\text{OH})_2$ [12], $\text{Ni}(\text{OH})_2$ [13], CaCO_3 [14], have been developed to cater for the template removal utilizing relatively gentle acid such as HCl.

Azo compounds have the functional group $\text{R}-\text{N}=\text{N}-\text{R}'$, in which R and R' can be either aryl or alkyl. As a consequence of π -delocalization, aryl azo compounds have vivid colors, especially reds, oranges, and yellows. Therefore, they are used as dyes, commonly known as azo dyes. The development of azo dyes was an important step in chemical industry. Taking tartrazine as an example, it is a synthetic lemon yellow azo dye primarily used as a food coloring, but also can be used with Brilliant Blue FCF or Green S to produce various green shades [15]. Considering the particular structure containing phenyls and especially high content nitrogen, tartrazine is for the first time expected to prepare nitrogen-doped porous carbon at elevated carbonization temperatures.

Herein, we present a straightforward carbonization method to prepare nitrogen-doped porous carbons without further physical or chemical activation, using tartrazine as carbon source and calcium acetate as hard template. The mass ratio of tartrazine and calcium acetate was emphatically investigated. The correlative capacitive performances were measured by cyclic voltammetry and galvanostatic charge–discharge techniques.

2. Experimental

All the analytical chemicals were purchased from Sinopharm Chemical Reagent (Shanghai) Co. Ltd. and used as received without further treatment.

In present experiment, pure tartrazine was heated at 800°C for 2 h under Ar flow to obtain **T-800-blank** sample. On the other hand, tartrazine and $\text{Ca}(\text{OAc})_2 \cdot \text{H}_2\text{O}$ with mass ratios of 1:1 and 3:1 at

800°C for 2 h under Ar flow to obtain **T-Ca-800-1:1/3:1** samples. The schematic routes and the unit structure of tartrazine are depicted in Fig. 1.

2.1. Typical synthetic procedure for **T-Ca-800-3:1** sample

Tartrazine and $\text{Ca}(\text{OAc})_2 \cdot \text{H}_2\text{O}$ powder (mass ratio of 3:1) were ground adequately and then placed in a porcelain boat, flushing with Ar flow for 30 min, and further heated in a horizontal tube furnace up to 800°C at a rate of 5°C min^{-1} and maintained at 800°C for 2 h under Ar flow. The resultant product was immersed with dilute HCl solution to remove soluble/insoluble substances, which was further washed with adequate deionized water until $\text{pH} = 7$. Finally, the sample was dried under vacuum at 120°C for 12 h to obtain the **T-Ca-800-3:1** sample.

Regarding the synthetic procedure for **T-Ca-800-1:1** sample, it is similar to that of **T-Ca-800-3:1** sample detailedly depicted above except for the mass ratio of tartrazine and $\text{Ca}(\text{OAc})_2 \cdot \text{H}_2\text{O}$ powder as 1:1.

Regarding the synthetic procedure for **T-Ca-blank** sample, it is similar to that of **T-Ca-800-3:1** sample without using $\text{Ca}(\text{OAc})_2 \cdot \text{H}_2\text{O}$.

2.2. Characterization

X-ray diffraction (XRD) patterns were obtained on a Rigaku D/MAX2500V with $\text{Cu K}\alpha$ radiation. Field emission scanning electron microscopy (FESEM) images were taken with a Hitachi S-4800 scanning electron microscope. X-ray photoelectron spectra (XPS) were obtained on a VG ESCALAB MK II X-ray photoelectron spectrometer with an exciting source of $\text{Mg K}\alpha$ (1253.6 eV). The specific surface area and pore structure of the carbon samples were determined by N_2 adsorption–desorption isotherms at 77 K (Quantachrome Autosorb-iQ) after being vacuum-dried at 150°C overnight. The specific surface areas were calculated by a BET (Brunauer–Emmett–Teller) method. Cumulative pore volume and pore-size distribution were calculated by using a slit/cylindrical nonlocal density functional theory (NLDFT) model.

2.3. Electrochemical measurements

In order to evaluate the capacitive performances of the as-prepared carbon samples (*ca.* 4 mg) in electrochemical capacitors, a mixture of 80 wt% the carbon powder, 15 wt% acetylene black and

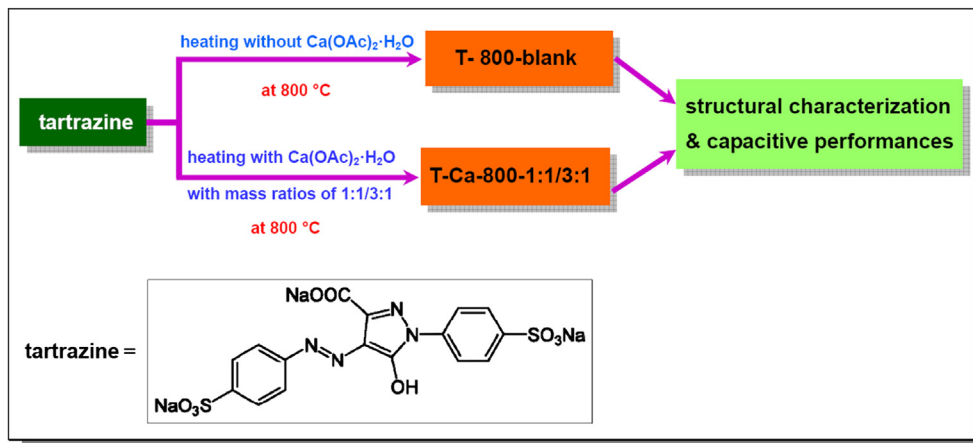


Fig. 1. Schematic illustration of the production of nitrogen-doped porous carbon by heating tartrazine with or without $\text{Ca}(\text{OAc})_2 \cdot \text{H}_2\text{O}$ at a designated carbonization temperature of 800°C for 2 h under Ar flow, in which $\text{Ca}(\text{OAc})_2 \cdot \text{H}_2\text{O}$ serves as hard template.

5 wt% polytetrafluoroethylene (PTFE) binder were fabricated using ethanol as a solvent. Slurry of the above mixture was subsequently pressed onto nickel foam under the pressure of 20 MPa, serving as a current collector. The prepared electrode was placed in a vacuum drying oven at 120 °C for 24 h. A three electrode experimental setup taking a 6 mol L⁻¹ KOH aqueous solution as electrolyte was used in cyclic voltammetry and galvanostatic charge–discharge measurements on an electrochemical working station (CHI660D, ChenHua Instruments Co. Ltd., Shanghai). Here, the prepared electrode, platinum foil (6 cm²) and saturated calomel electrode (SCE) were used as the working, counter and reference electrodes, respectively.

Specific capacitances derived from galvanostatic tests can be calculated from the equation:

$$C = \frac{I\Delta t}{m\Delta V}$$

where C (F g⁻¹) is the specific capacitance; I (A) is the discharge current; Δt (s) is the discharge time; ΔV (V) is the potential window; and m (mg) is the mass of active materials loaded in working electrode.

Specific energy density (E) and specific power density (P) derived from galvanostatic tests can be calculated from the equations:

$$E = \frac{1}{2} C \Delta V^2$$

$$P = \frac{E}{\Delta t}$$

where E (Wh kg⁻¹) is the average energy density; C (F g⁻¹) is the specific capacitance; ΔV (V) is the potential window; P (W kg⁻¹) is the average power density and Δt (s) is the discharge time.

3. Results and discussion

The component, crystallinity and purity of the carbon samples were studied by XRD technique. By direct carbonization of pure tartrazine at 800 °C for 2 h under Ar flow, black product appears and the corresponding XRD pattern is shown in Fig. 2a, mainly consisting of carbon, orthorhombic Na₂SO₄ (JCPDS Card No. 37-0808) and other unidentified substances. The formation of Na₂SO₄ originates from the reaction of sulfonate and sodium ions within the structure of tartrazine, and similar phenomenon also occurs in case of production of porous carbon from calcium lignosulfonate [16]. The product was subsequently washed with aqueous HCl solution and deionized water to remove any soluble/insoluble

impurities, resulting in the formation of relatively pure carbon, dominated as **T-800-blank**. The XRD pattern in Fig. 2b has one broad diffraction peak centering at ca. 24.9°, indicative feature of amorphous carbon and close to that of (002) plane of crystal graphite. Furthermore, one minor and indistinct diffraction peak locates at ca. 24.9°, approximately indexed as (10) plane [17]. On the other hand, when heating the mixture of tartrazine and Ca(OAc)₂·H₂O powder as 1:1/3:1 at 800 °C, the product is composed of amorphous carbon and CaCO₃, CaO etc. [18], which was washed with aqueous HCl solution and deionized water, eventually resulting in **T-Ca-800-1:1/3:1**. Their XRD patterns are shown in Fig. 2d–e, incredibly close to that of **T-800-blank**.

The shapes and sizes of the carbon samples were investigated by FESEM technique. Fig. 3a shows the representative FESEM image of the **T-800-blank** sample, which consists of a large number of micrometer block particles with irregular shapes. With respect to **T-Ca-800-1:1/3:1** samples, their FESEM images depicted in Fig. 3b–d are somewhat similar to that of **T-800-blank**. Taking into account the self-carbonization/decomposition of tartrazine as well as the templating effect of calcium acetate at elevated temperatures, nanoscale porous structures are anticipated to happen within the carbon products, which will further be detected by the following N₂ adsorption/desorption analysis.

The empirical composition, functional groups on the surfaces, chemical state and electronic state of the elements toward the present carbons were determined by XPS technique, giving information concerning the outermost 3–4 nm surface layer carbon surface. Fig. 4a indicates the overall XPS survey spectra of the **T-800-blank** and **T-Ca-800-1:1/3:1** samples from 0 to 1400 eV. All the carbon samples consisting of C/N/O elements apparently reveal their purities after washing process. In addition, the relative intensities of C/N/O elements differentiate from each other, implying their different content in the products. The high resolution XPS spectra toward C1s are given in Fig. 4b, ranging from 280.5 to 297.5 eV, which can be closely fitted into three main peaks locating at ca. 284.9, 285.8 and 288.3 eV, respectively. In details, the peak at ca. 284.9 eV is attributed to sp² C=C bond, evincing the graphitic nature [19]. The peak at ca. 285.8 eV might be due to sp³ C–C bond [20] and/or C–N bond [21]. As for the one at ca. 288.3 eV, it can be incurred by –O–C=O bond [22].

Fig. 4c gives us the high resolution XPS spectra of O1s with the binding energy scope from 526.5 to 541.0 eV. All the O1s spectra are almost the same and can be approximately fitted into three main peaks at ca. 531.4, 532.5 and 533.4 eV, respectively. Hereinto, the peak at ca. 531.4 eV owes to –C=O bond; the peak at ca. 532.5 eV is due to C–O–C/C–OH bond; and the one at ca. 533.4 eV can be ascribed to O–C=O bond [23]. Besides, the high resolution N1s

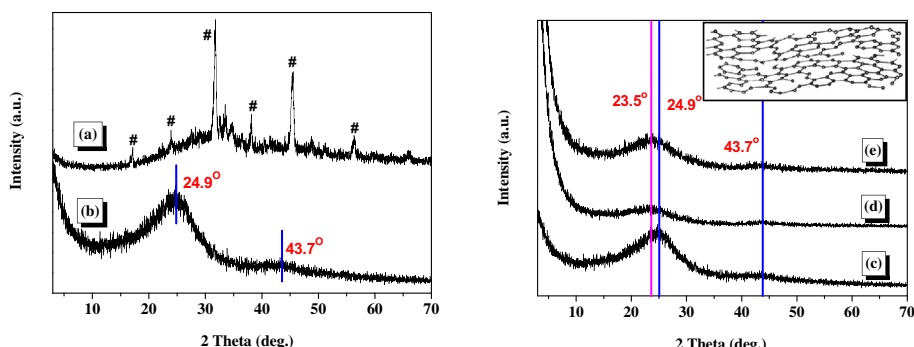


Fig. 2. XRD patterns of the **T-800-blank** sample before (a) and after (b) being washed with aqueous HCl solution and deionized water to remove any unwanted impurities; as well as the comparative XRD patterns of the (c) **T-800-blank**; (d) **T-Ca-800-1:1** and (e) **T-Ca-800-3:1** samples. Notes: # = orthorhombic Na₂SO₄ (JCPDS Card No. 37-0808). The inset in the right XRD pattern is the approximate unit structure of amorphous carbon.

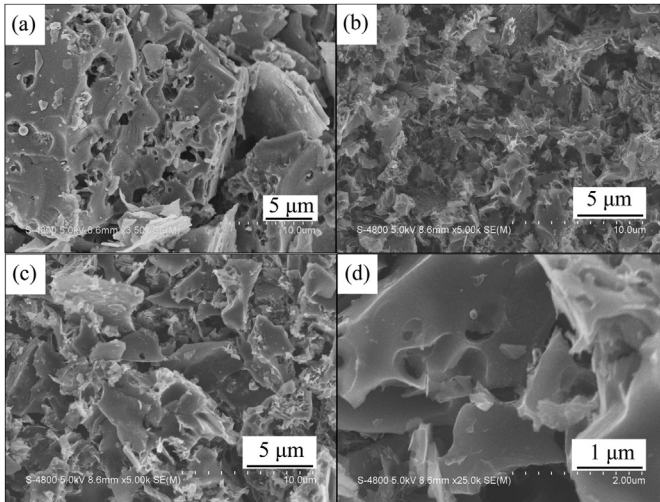


Fig. 3. FESEM images of the carbon samples: (a) T-800-blank; (b) T-Ca-800-1:1 and (c–d) T-Ca-800-3:1.

spectra (393.0–410.0 eV) of the carbon samples are depicted in Fig. 4d, which are also fitted into three main peaks locating at *ca.* 398.6, 400.3 and 401.4 eV, respectively. Furthermore, as is indicated in Fig. 4e, there exists four types of nitrogen species within

Table 1
XPS peak analysis of the carbon samples.

Sample	C (at.%)	N (at.%)	O (at.%)
T-800-blank	82.95	6.77	10.28
T-Ca-800-1:1	87.73	3.06	9.21
T-Ca-800-3:1	87.51	3.41	9.08

nitrogen-doped carbon, including pyridinic nitrogen (398.6 ± 0.3 eV), pyrrolic nitrogen (400.5 ± 0.3 eV), graphitic nitrogen (also as quaternary nitrogen, 401.3 ± 0.3 eV), oxidized pyridinic nitrogen (402–405 eV) [16–18]. Therefore, the peaks at Fig. 4d can orderly be attributed to pyridinic nitrogen, pyrrolic nitrogen and graphitic nitrogen. The total XPS peak analysis of the carbon samples are summarized in Table 1. It is clearly seen that the **T-800-blank** sample displays higher content of nitrogen species than that of the **T-Ca-800-1:1/3:1** samples. The contents of C/N/O elements listed in Table 1 are to some extent consistent with the relative intensities shown in Fig. 4a.

The surface areas and pore structures of the carbon samples were investigated by N_2 adsorption–desorption isotherms and pore size distributions calculated by using a slit/cylindrical NLDFT model. Fig. 5a represent the typical N_2 adsorption–desorption isotherms of **T-800-blank** and **T-Ca-800-1:1/3:1** samples, demonstrating the similar trends in shapes with relative pressure (P/P_0) ranging from 0 to 1.0. According to the classification of adsorption–

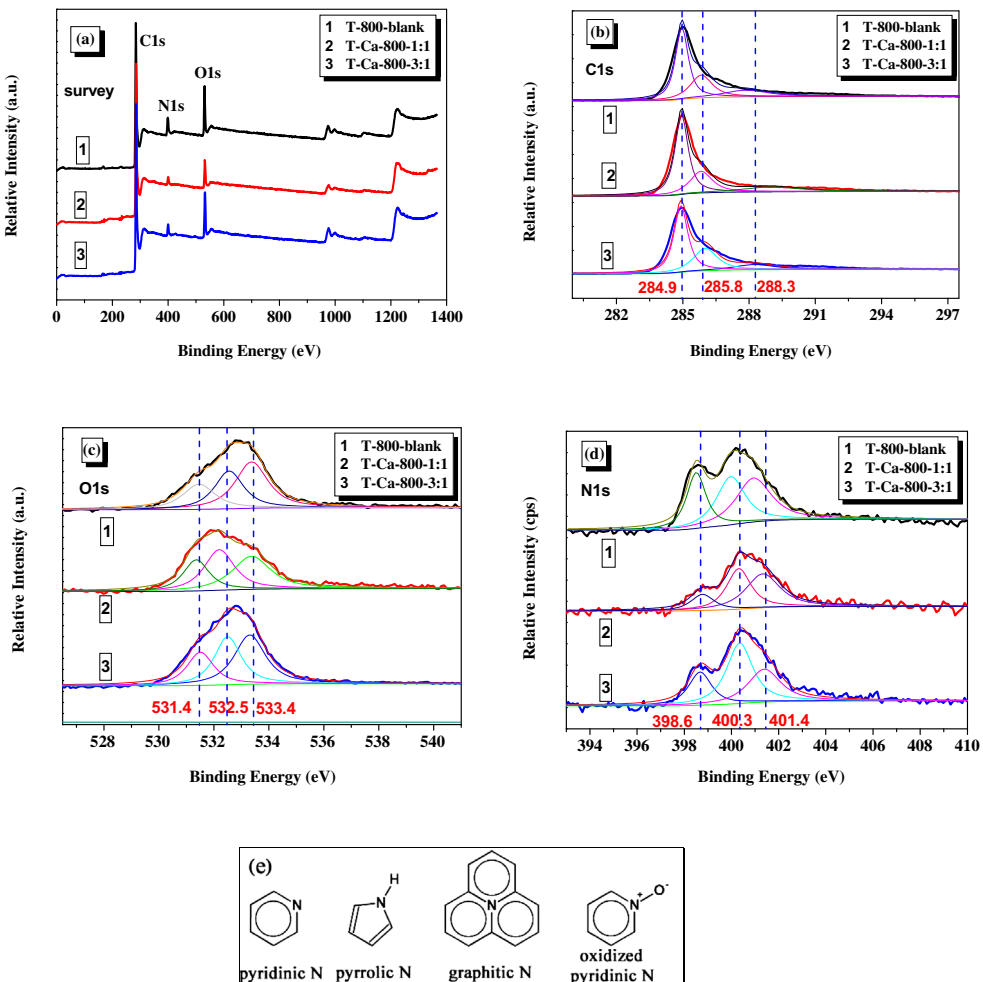


Fig. 4. XPS spectra of the carbon samples: (a) survey; (b) C1s; (c) O1s; (d) N1s and (e) four types of nitrogen species commonly reported in nitrogen-doped carbon materials.

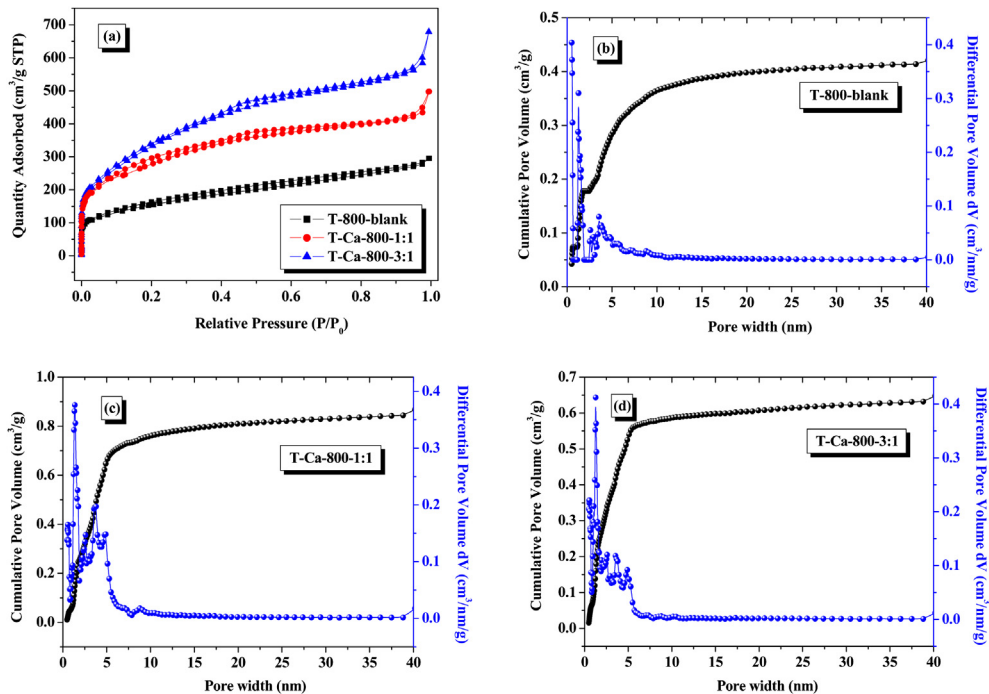


Fig. 5. (a) N₂ adsorption–desorption isotherms and (b–d) cumulative pore volume and pore-size distribution (calculated by using a slit/cylindrical NLDFT model).

desorption isotherms defined by IUPAC, the isotherms shown in Fig. 5a can be ascribed to the combination of types I and IV [24]. The sharp increases at low relative pressure ($<0.4 P/P_0$) indicate the existence of micropores; the hysteresis loops at medium relative pressure (0.4–1.0 P/P_0) reveal the existence of developed mesopores; and the closely vertical tails at high pressure ($\sim 1.0 P/P_0$) demonstrate the presence of macroporosity [25,26]. This kind of hierarchical pore structures are also confirmed by the pore size distribution curves, especially in microscale scopes below 2 nm, in which a hybrid nonlocal DFT (NLDFT) kernel from nitrogen adsorption was applied. It assumes a slit pore geometry for micropores and a cylindrical pore geometry for mesopores. The resultant cumulative pore volumes and pore size analysis of the carbon samples are given in Fig. 5b–d, further depicting multimodal pore structures expressly in the scope of 0.5–6 nm.

The total surface areas and pore structures of the carbon samples are summarized in Table 2. In details, the **T-800-blank** sample exhibits BET surface area of $861 \text{ m}^2 \text{ g}^{-1}$ and total pore volume $0.47 \text{ cm}^3 \text{ g}^{-1}$. Interestingly, the BET surface area and total pore volume of the **T-Ca-800-1:1** sample has greatly increased up to $1430 \text{ m}^2 \text{ g}^{-1}$ and $0.84 \text{ cm}^3 \text{ g}^{-1}$, respectively. It proves that the addition of $\text{Ca(OAc)}_2 \cdot \text{H}_2\text{O}$ indeed favors for enlarging/adjusting the pore structures within carbons. In particular, the **T-Ca-800-3:1** sample possesses the high BET surface area of $1669 \text{ m}^2 \text{ g}^{-1}$ and total pore volume of $0.85 \text{ cm}^3 \text{ g}^{-1}$, which are much higher than the previously reported values assisted with the templates of MgO [11].

CaCO_3 [14] and zeolitic imidazolate framework (ZIF-8) [27]. Of course, the Na_2SO_4 produced by the carbonization of tartrazine at elevated temperature also serves as pore-forming agent to some extent. On the other hand, taking the **T-Ca-800-3:1** sample as an example, the measured BET surface area of $1669 \text{ m}^2 \text{ g}^{-1}$ includes the micropore area of $434 \text{ m}^2 \text{ g}^{-1}$ and the external surface area of $1235 \text{ m}^2 \text{ g}^{-1}$; the total pore volume of $0.85 \text{ cm}^3 \text{ g}^{-1}$ includes micropore volume $0.18 \text{ cm}^3 \text{ g}^{-1}$ and meso-/macro-pore volume of $0.67 \text{ cm}^3 \text{ g}^{-1}$, clearly suggesting small contribution from micropores but large from meso-/macro-pores.

Cyclic voltammetry (CV) is one of the most commonly used electrochemical techniques, and is based on a linear potential waveform, showing the current vs. a varying applied potential. Fig. 6 demonstrates the cyclic voltammograms of the **T-800-blank** and **T-Ca-800-1:1/3:1** samples at various scan rates ranging from 10 to 400 mV s^{-1} . At a low scan rate of 10 mV s^{-1} , the CV curves in Fig. 6a display almost rectangular shapes in a potential range of -1.0 – 0 V , confirmation of good double layer capacitive behavior, low equivalent series resistance (ESR) and the fast diffusion of electrolyte ions into the composite [28]. Secondly, the absence of any redox humps reveals little contribution from redox reaction. Thirdly, it is seen in Fig. 6a that the **T-Ca-800-3:1** sample exhibits the largest specific capacitance but the **T-800-blank** sample exhibits the smallest one because the capacitance is proportional to the integral area surrounded by CV curve [29]. Moreover, faster scan rates especially beyond 400 mV s^{-1} make the resultant CV

Table 2

Characteristic surface areas and pore structures of the carbon samples.

Sample	BET surface area ($\text{m}^2 \text{ g}^{-1}$)			Langmuir surface area ($\text{m}^2 \text{ g}^{-1}$)	Total pore volume ($\text{cm}^3 \text{ g}^{-1}$)	Micropore volume ($\text{cm}^3 \text{ g}^{-1}$)	Average pore width (nm)
	Total	S_{micro}	S_{ext}				
T-800-blank	861	279	582	1176	0.47	0.12	2.2
T-Ca-800-1:1	1430	216	1214	1975	0.84	0.08	2.4
T-Ca-800-3:1	1669	434	1235	2294	0.85	0.18	2.0

Notes: 1. S_{micro} represents the micropore area calculated by t -plot; 2. S_{ext} represents the external surface area calculated by t -plot.

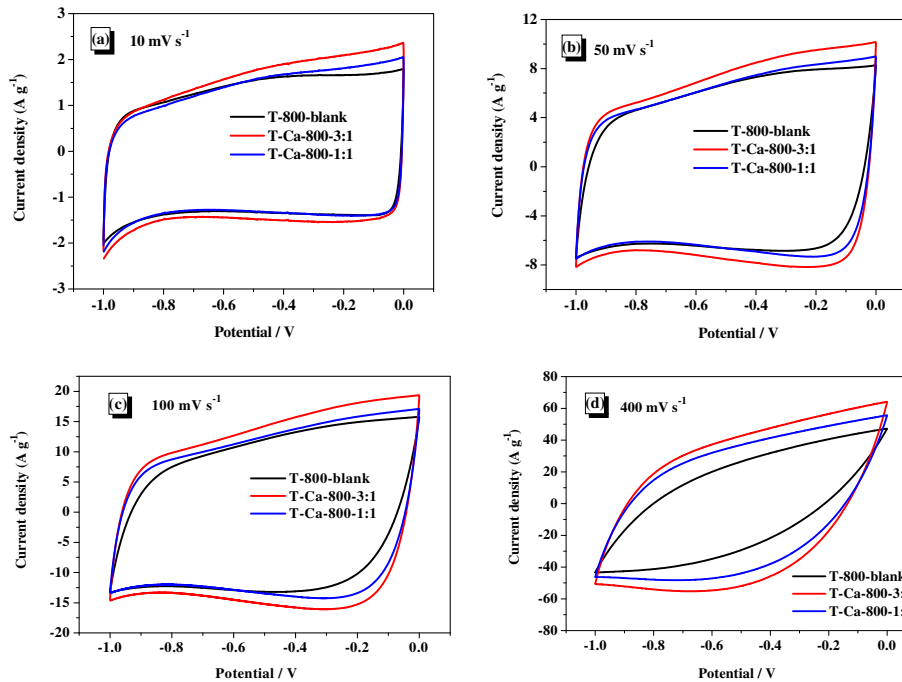


Fig. 6. Cyclic voltammograms of the T-800-blank, T-Ca-800-1:1 and T-Ca-800-3:1 samples at various scan rates: (a) 10 mV s^{-1} ; (b) 50 mV s^{-1} ; (c) 100 mV s^{-1} and (d) 400 mV s^{-1} .

curves more deteriorated, far from ideal rectangles, as illustrated in Fig. 6d.

The T-Ca-800-1:1 sample is in-depth investigated due to the excellent electrochemical behavior, as given in Fig. 6, primarily derived from its high BET surface area, total pore volume and

hierarchical pore structures and rational nitrogen content. Fig. 7a indicates the T-Ca-800-3:1 sample's cyclic voltammograms at the scan rates from 10 to 800 mV s^{-1} , accompanying with the increase of integral area and worse deviation from ideal rectangle. This is incurred by the insufficient ion diffusion at high scan rate,

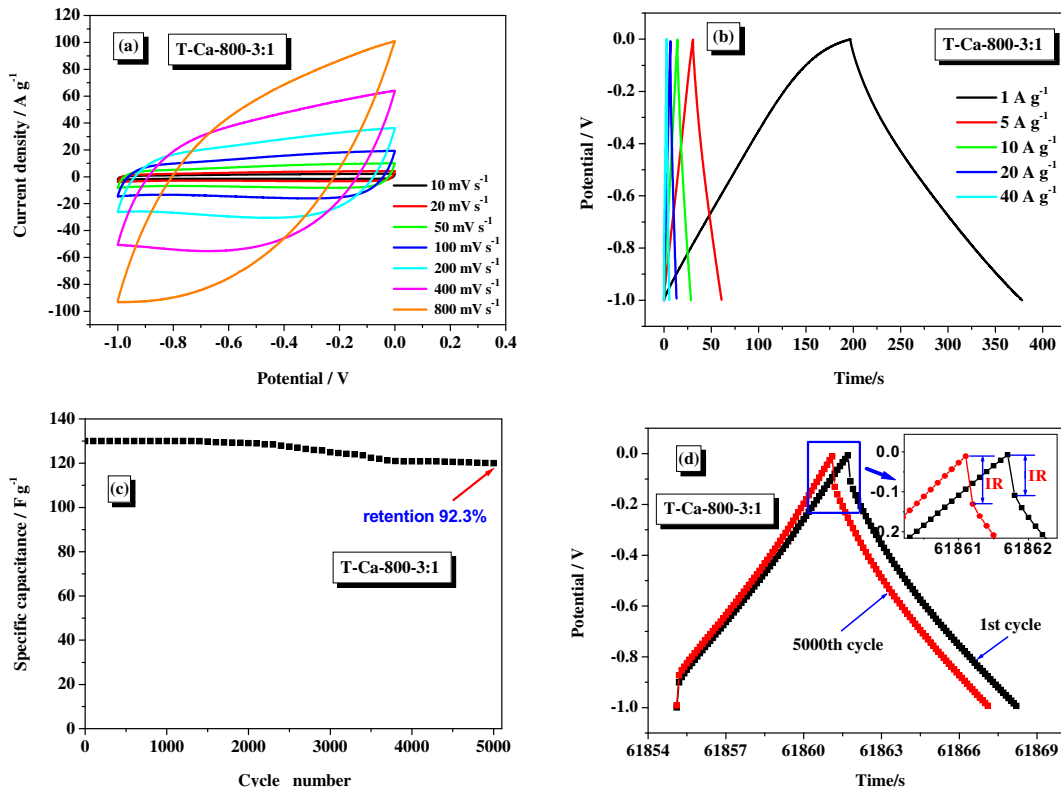


Fig. 7. The T-Ca-800-3:1 sample: (a) cyclic voltammograms at various scan rates; (b) galvanostatic charge–discharge curves measured at various current densities; (c) cycling stability at the current density of 20 A g^{-1} ; (d) galvanostatic charge–discharge curves of the 1st and 5000th cycles.

particularly exceeding 400 mV s^{-1} hereinto. Besides, galvanostatic charge–discharge technique is also commonly used to study the electrochemical performance. Fig. 7b shows the total galvanostatic charge–discharge curves measured at current densities ranging from 1 to 40 A g^{-1} , in which all curves exhibit nearly triangle in shapes, proving their excellent double layer capacitance behavior.

Long-term cycling behavior is a major premise for practical application of supercapacitors. To realize this purpose, the specific capacitance as a function of cycle number is given in Fig. 7c, maintaining the current density at 20 A g^{-1} in the test process. As a result, it is of significance toward the **T-Ca-800-3:1** sample that high capacitance retention of *ca.* 92.3% retains within 5000 cycles (that is to say, only *ca.* 7.7% loss), apparently indicating its good stability, lifetime and a very high degree of reversibility in the repetitive charge–discharge cycling. The corresponding galvanostatic charge–discharge curves of the 1st and 5000th cycles are displayed

in Fig. 7d. Owing to the enhancement of internal resistance, IR drop, also called voltage drop, therefore increases along with the augmentation of charge–discharge cycles [30], as pointed out in the inset of Fig. 7d.

The electrochemical behaviors of **T-800-blank** and **T-Ca-800-1:1/3:1** samples were further studied in a comparative manner. Fig. 8a displays the galvanostatic charge–discharge curves measured at the current density of 1 A g^{-1} , and all of them exhibit nearly triangular shapes in a potential range of -1.0 – 0 V .

The specific capacitances at the current densities from 0.5 to 60 A g^{-1} are plotted in Fig. 8b. Panoramic view hereinto tells us that the **T-Ca-800-3:1** sample takes on the best specific capacitance and the largest one is 224.3 F g^{-1} obtained at 0.5 A g^{-1} . The capacitance retention is *ca.* 63.8% at 10 A g^{-1} and *ca.* 42.6% even at high current density of 60 A g^{-1} , which are much larger than those of commonly reported carbons [31,32]. The high capacitance retention toward

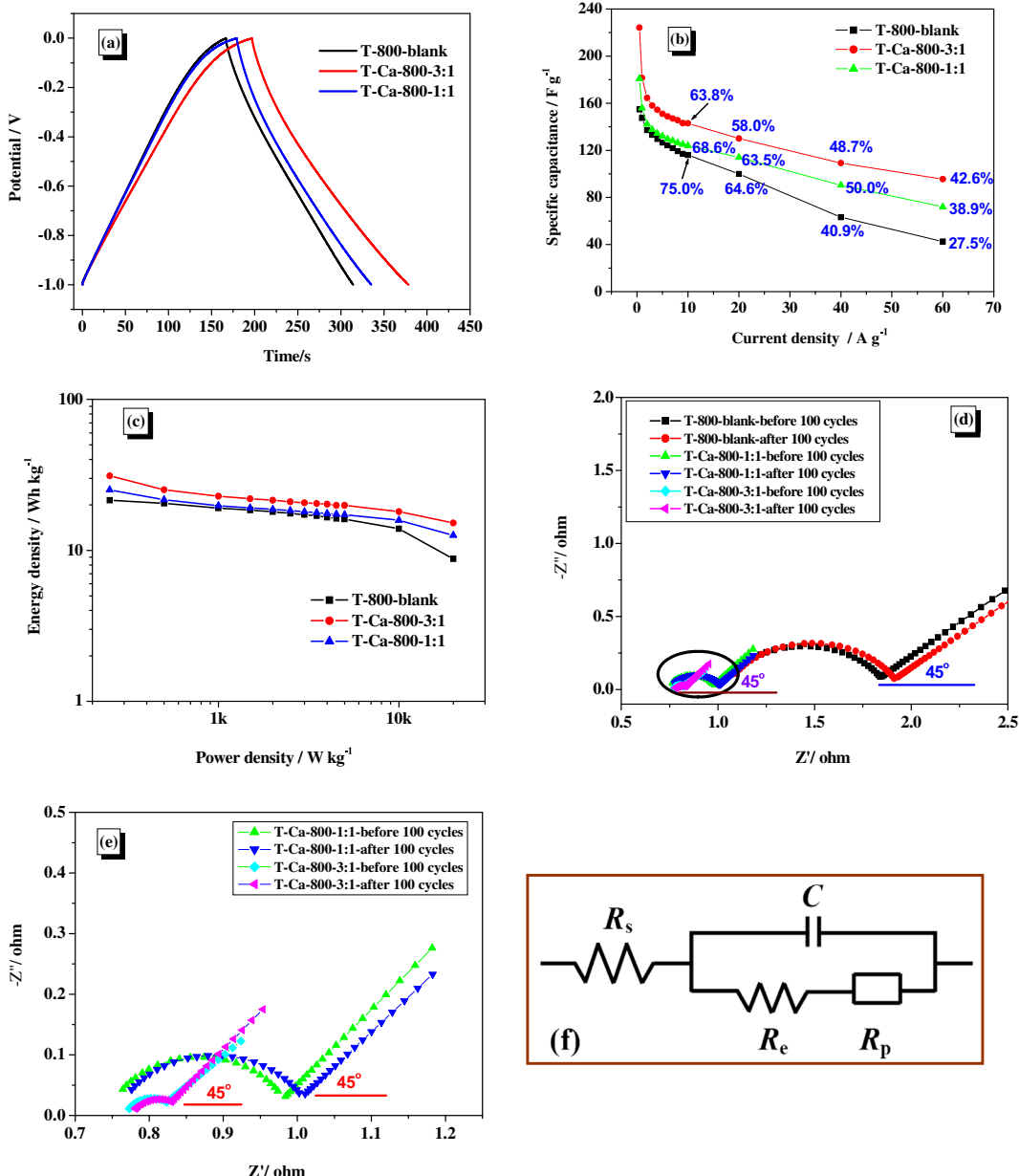


Fig. 8. (a) Galvanostatic charge–discharge curves measured at the current density of 1 A g^{-1} ; (b) Specific capacitances at various current densities; (c) Ragone plots showing energy density vs. power density; (d–e) Nyquist plots before/after 100 cycles of the carbon samples; (f) The equivalent circuit model for the circuit plot.

Table 3

The overall resistance (R_t), electrical connection resistance (R_e), electrolyte resistance (R_s), and resistance of ion migration in carbon micropores (R_p) of the carbon samples.

Samples	Resistance (Ohm)			
	R_t	R_s	R_e	R_p
T-800-blank-before cycling	2.4838	1.0649	0.7737	0.6452
T-800-blank-after 100 cycles	2.5272	1.0897	0.8222	0.6153
T-Ca-800-1:1-before cycling	1.1821	0.7645	0.2197	0.1979
T-Ca-800-1:1-after 100 cycles	1.1829	0.7761	0.2265	0.1803
T-Ca-800-3:1-before cycling	0.9239	0.7729	0.0506	0.1003
T-Ca-800-3:1-after 100 cycles	0.9534	0.7810	0.0489	0.1235

the **T-Ca-800-3:1** sample is induced by not only the high BET surface area and total pore volume, generating a high electrode/electrolyte contact area and short path lengths for electronic transport and electrolyte ion, but also the nitrogen-doping within carbons, improving faradic reactions of the nitrogen-containing functional groups or wettability of the pore walls [32].

The overall Ragone plots of the present carbon samples are shown in Fig. 8c. Obviously, the highest energy density & power density values can be achieved toward the **T-Ca-800-3:1** sample. Detailedly, it displays a high energy density of *ca.* 31.2 W h kg⁻¹ at a power density of *ca.* 0.25 kW kg⁻¹; a high power density of *ca.* 20 kW kg⁻¹ at an energy density of *ca.* 15.2 W h kg⁻¹. Besides, the most important challenge toward supercapacitors facing today is to increase the device energy density to reach 10 W h kg⁻¹ or more, moving them closer to batteries and cutting the cost at the same time [33]. It is therefore concluded that the present carbons, especially the case of **T-Ca-800-3:1** sample, are expected to be excellent candidates for supercapacitor electrode materials.

Nyquist plots, also named electrochemical impedance spectroscopy (EIS), showing real impedance vs. imaginary impedance, are indicated in Fig. 8d–e, applying a sine wave with amplitude of 5.0 mV in the frequency range of 100 kHz to 0.01 Hz. In present work, these Nyquist plots are measured before/after 100 cycles and further fitted by ZView software. Each Nyquist plot is composed of a depressed semicircle in the high frequency region and a straight line, also called Warburg resistance having slope of the 45°, in the low frequency region. Furthermore, based on the radii of semicircles at the X-axis (*i.e.*, real axis), as depicted in Fig. 8d, we can see that the **T-Ca-800-3:1** sample takes the smallest inter-granular electrical resistance between the carbon particles derived from the electrode surface area and the inter-particle resistivity [34], while the **T-800-blank** takes the largest one. The Warburg curves tell us that the order of the ion diffusion paths are as follows [35]: **T-Ca-800-3:1** < **T-Ca-800-1:1** < **T-800-blank**. Meanwhile, the equivalent series resistances (ESR), determining the charge–discharge rate of present carbons, also have the similar order, concluded from the X-intercept of the Nyquist plots in Fig. 8d [36]. Certainly, the short ion diffusion paths as well as small ESR data facilitate the efficient access of electrolyte ions to the pore surfaces, which makes the **T-Ca-800-3:1** sample exhibit the best capacitive behavior. Finally, the Nyquist plots are fitted by equivalent circuit model, as scheduled in Fig. 8f, consisting of electrical connection resistance (R_e), electrolyte resistance (R_s) and resistance of ion migration in carbon micropores (R_p), as well as overall resistance (R_t), and the resulting values are listed in Table 3.

4. Conclusions

In summary, a direct and efficient carbonization method has been employed to prepare nitrogen-doped porous carbons, in which tartrazine and $\text{Ca(OAc)}_2 \cdot \text{H}_2\text{O}$ acts as carbon source and hard

template, respectively. With the help of $\text{Ca(OAc)}_2 \cdot \text{H}_2\text{O}$, the carbons can possess high surface area and large total pore volume. As far as **T-Ca-800-3:1** sample is concerned, it has the highest BET surface area as 1669 m² g⁻¹ and largest total pore volume 0.85 cm³ g⁻¹, and also exhibits excellent capacitive behaviors for the application of supercapacitor.

It is believed that several scientific advantages happen as follows: (1) The tartrazine used is inexpensive and can supply nitrogen species incorporated into porous carbon, fairly benefit for improving the capacitive performances. (2) The addition of $\text{Ca(OAc)}_2 \cdot \text{H}_2\text{O}$ can evidently enhance the BET surface area and total pore volume. Compared with the pristine **T-800-blank** sample (BET surface area as 861 m² g⁻¹ and total pore volume 0.47 cm³ g⁻¹), the **T-Ca-800-1:1** sample has increased up to 1430 m² g⁻¹ and 0.84 cm³ g⁻¹, and the **T-Ca-800-3:1** sample has increased up to 1669 m² g⁻¹ and 0.85 cm³ g⁻¹. (3) The **T-Ca-800-3:1** sample exhibits excellent capacitive performances, such as high rate capability (the retention of 42.6% even at high current density of 60 A g⁻¹) and long cycling stability (the loss of 7.7% within 5000 cycles).

The present carbonization method is expected to convert other kinds of azo dyes into nitrogen-doped porous carbons, especially possessing high surface areas, large pore volumes and the resultant excellent capacitive behaviors.

Acknowledgments

This work was supported by Anhui Province Key Laboratory of Environment-friendly Polymer Materials, Anhui University, Hefei 230039, China (KF2012009). Dr. Xiang Ying Chen also thanks the financial support from the National Natural Science Foundation of China (21101052) and China Postdoctoral Science Foundation (20100480045).

References

- [1] L.L. Zhang, X.S. Zhao, Chem. Soc. Rev. 38 (2009) 2520–2531.
- [2] E. Frackowiak, F. Béguin, Carbon 39 (2001) 937–950.
- [3] P. Simon, Y. Gogotsi, Nat. Mater. 7 (2008) 845–854.
- [4] Y.P. Zhai, Y.Q. Dou, D.Y. Zhao, P.F. Fulvio, R.T. Mayes, S. Dai, Adv. Mater. 23 (2011) 4828–4850.
- [5] M. Inagaki, H. Konno, O. Tanaike, J. Power Sources 195 (2010) 7880–7903.
- [6] R. Lin, P.L. Taberna, S. Fanti, V. Presser, C.R. Pérez, F. Mabosc, N.L. Rupesinghe, K.B.K. Teo, Y. Gogotsi, P. Simon, J. Phys. Chem. Lett. 2 (2011) 2396–2401.
- [7] P. Simon, Y. Gogotsi, Acc. Chem. Res. (2012), <http://dx.doi.org/10.1021/ar200306b>. ASAP.
- [8] J. Lee, J. Kim, T. Hyeon, Adv. Mater. 18 (2006) 2073–2094.
- [9] B. Xu, F. Wu, S. Chen, Z. Zhou, G. Cao, Y. Yang, Electrochim. Acta 54 (2009) 2185–2189.
- [10] Y.D. Xia, Z.X. Yang, R. Mokaya, Nanoscale 2 (2010) 639–659.
- [11] T. Morishita, T. Tsumura, M. Toyoda, J. Przepiórski, A.W. Morawski, H. Konno, M. Inagaki, Carbon 48 (2010) 2690–2707.
- [12] D.W. Wang, F. Li, L.C. Yin, X. Lu, Z.G. Chen, I.R. Gentle, G.Q. Lu, H.M. Cheng, Chem. Eur. J. 18 (2012) 5345–5351.
- [13] D.W. Wang, F. Li, M. Liu, G.Q. Lu, H.M. Cheng, Angew. Chem. Int. Ed. 47 (2008) 373–376.
- [14] B. Xu, L. Peng, G. Wang, G. Cao, F. Wu, Carbon 48 (2010) 2361–2380.
- [15] A. Axon, F.E.B. May, L.E. Gaughan, F.M. Williams, P.G. Blain, M.C. Wright, Toxicology 298 (2012) 40–51.
- [16] X.Y. Chen, Q.Q. Zhou, Electrochim. Acta 71 (2012) 92–99.
- [17] Z.Q. Li, C.J. Lu, Z.P. Xia, Y. Zhou, Z. Luo, Carbon 45 (2007) 1686–1695.
- [18] T.J. Schwartz, A.R.P. van Heiningen, M.C. Wheeler, Green Chem. 12 (2010) 1353–1356.
- [19] T.I.T. Okpalugo, P. Papakonstantinou, H. Murphy, J. McLaughlin, N.M.D. Brown, Carbon 43 (2005) 153–161.
- [20] S.K. Jerng, D.S. Yu, J.H. Lee, C. Kim, S. Yoon, S.H. Chun, Nanoscale Res. Lett. 6 (2011) 565–570.
- [21] T. Ramanathan, F.T. Fisher, R.S. Ruoff, L.C. Brinson, Chem. Mater. 17 (2005) 1290–1295.
- [22] V. Datsyuk, M. Kalyva, K. Papagelis, J. Parthenios, D. Tasis, A. Siokou, I. Kallitsis, C. Gallois, Carbon 46 (2008) 833–840.
- [23] C. Pevida, T.C. Drage, C.E. Snape, Carbon 46 (2008) 1464–1474.

[24] W.H. Suh, J.K. Kang, Y.H. Suh, M. Tirrell, K.S. Suslick, G.D. Stucky, *Adv. Mater.* 23 (2011) 2332–2338.

[25] F. Xu, R. Cai, Q. Zeng, C. Zou, D. Wu, F. Li, X. Lu, Y. Liang, R. Lu, *J. Mater. Chem.* 21 (2011) 1970–1976.

[26] B. Liu, H. Shioyama, T. Akita, Q. Xu, *J. Am. Chem. Soc.* 130 (2008) 5390–5391.

[27] W. Chaikittisilp, M. Hu, H. Wang, H.S. Huang, T. Fujita, K.C.W. Wu, L.C. Chen, Y. Yamauchi, K. Ariga, *Chem. Commun.* 48 (2012) 7259–7261.

[28] W.W. Liu, X.B. Yan, J.W. Lang, C. Peng, Q.J. Xue, *J. Mater. Chem.* 22 (2012) 17245–17253.

[29] Y. Li, X. Zhao, Q. Xu, Q. Zhang, D. Chen, *Langmuir* 27 (2011) 6458–6463.

[30] J. Li, H. Xie, Y. Li, J. Liu, Z. Li, *J. Power Sources* 196 (2011) 10775–10781.

[31] J. Zhou, X. Yuan, W. Xing, W. Si, S. Zhuo, *Carbon* 48 (2010) 2765–2772.

[32] L.F. Chen, X.D. Zhang, H.W. Liang, M.G. Kong, Q.F. Guan, P. Chen, Z.Y. Wu, S.H. Yu, *ACS Nano* 6 (2012) 7092–7102.

[33] L.L. Zhang, X. Zhao, H. Ji, M.D. Stoller, L. Lai, S. Murali, S. McDonnell, B. Clevenger, R.M. Wallace, R.S. Ruoff, *Energy Environ. Sci.* 5 (2012) 9618–9625.

[34] A. Burke, *Electrochim. Acta* 53 (2007) 1083–1091.

[35] Q. Cheng, J. Tang, J. Ma, H. Zhang, N. Shinya, L.C. Qin, *Carbon* 49 (2011) 2917–2925.

[36] Y. Wang, Z. Shi, Y. Huang, Y. Ma, C. Wang, M. Chen, Y. Chen, *J. Phys. Chem. C* 113 (2009) 13103–13107.